Photocatalytic self-cleaning graphene oxide/ZnO hybrid membrane for ultrafast cyclic small organic molecule separation

Journal of Membrane Science 697 (2024) 122539

Contents lists available at ScienceDirect

Journal of Membrane Science

journal homepage: www.elsevier.com/locate/memsci

Photocatalytic self-cleaning graphene oxide/ZnO hybrid membrane for ultrafast cyclic small organic molecule separation

Nurul A. Mazlan [a], Allana Lewis [a], Zheng Chen [a], Fraz Saeed Butt [a], Jilong Han [b,**], Norbert Radacsi [a], Shuiqing Yang [c,***], Yi Huang [a,*]

[a] School of Engineering, Institute for Materials & Processes, The University of Edinburgh, Robert Stevenson Road, Edinburgh, EH9 3FB, UK
[b] School of Chemical and Pharmaceutical Engineering, Hebei University of Science and Technology, Shijiazhuang, China
[c] Jiangsu Dingying New Materials Co., Ltd., Changzhou, Jiangsu, 213031, China

ARTICLE INFO

Keywords:
Photocatalytic
Self-cleaning
Graphene oxide
ZnO
Hybrid membrane

ABSTRACT

Graphene oxide (GO) based membranes have attracted tremendous interest owing to their unique lamellar structure resulting in excellent molecular filtration. However, the expansion of interlayer spacing of GO nanoflakes in liquid solutions, particularly in aqueous solution, and the adsorption of foulants in the layered nanoconfinement as well as on the surface adversely affects the long-term performance of the membranes. In this work, one-dimensional zinc oxide (ZnO) nanorods were integrated with graphene oxide via in-situ crystallization. A fast thermal treatment was applied to partially reduce the graphene oxide nanoflakes and chemically 'lock' the newly formed ZnO nanorods during the final step of hybrid membrane fabrication. It was found that the partially reduced graphene oxide (rGO) provided excellent mechanical stability between the nanolayers and also very stable and efficient molecular sieving properties. Interestingly, the ZnO nanorods not only served as a space holder between neighbouring reduced graphene-oxide nanoflakes but also endowed the hybrid membrane with responsive photocatalytic self-cleaning properties, which has been considered one of the most promising approaches for energy-efficient environmental remediation. In water permeation tests, these graphene oxide-zinc oxides (P-rGO/ZnO) membranes exhibited ultrahigh permeance of 400 ± 21 L m^{-2} h^{-1} bar^{-1}, more than an order of magnitude higher than the conventional rGO membranes. In the meantime, these membranes exhibited excellent small organic molecule separation efficiencies with >98.8 ± 1.2% rejections toward direct red 80, rose bengal, reactive black 5, and trypan blue. More importantly, under ultraviolet–visible light irradiation, the membrane demonstrated highly efficient self-cleaning behaviour for fast organic dye decomposition, enabling excellent cyclic removal of pre-adsorbed dye molecules. Therefore, this intelligent self-cleaning hybrid membrane has great potential in wastewater purification, particularly for ultrafast small organic molecule removal.

1. Introduction

Rapid industrial development, urbanization, and population growth have caused environmental pollution leading to water scarcity problems [1,2]. Water pollution has recently been particularly prominent due to the increasing demand for freshwater [3,4]. One of the major dangerous contaminants is organic dyes that have been produced in large quantities by textile [5–7], paint [8], leather and paper industries [9–11]. Most organic dyes are highly toxic, carcinogenic, and non-biodegradable [12,13]. Thus, the presence of dyes is not only harmful to public health but also causes a deleterious effect on aquatic organisms [14,15]. Therefore, it is important to minimise these pollutants by efficiently extracting them either directly from the source or from the environment. To date, various conventional technologies such as adsorption [16,17], distillation [18,19], flocculation [20], biodegradation [21,22] and advanced oxidation processes [23–25], are broadly implemented in the industrial sector to remove organic dyes from water. Nevertheless, the major drawback of these techniques is the production of secondary pollutants which requires subsequent treatment of the toxic sludge produced, further increasing the operation cost [26,27].

* Corresponding author.
** Corresponding author.
*** Corresponding author.
E-mail addresses: hanjilong@hebust.edu.cn (J. Han), dingyingmaterial@163.com (S. Yang), yi.huang@ed.ac.uk (Y. Huang).

https://doi.org/10.1016/j.memsci.2024.122539
Received 4 October 2023; Received in revised form 25 January 2024; Accepted 4 February 2024
Available online 14 February 2024

Recently, among various water treatment technologies, membrane technology has earned tremendous attention over time due to its low energy consumption, cost-efficiency, reduced chemical usage, and reduction in the processing stages [28]. More specifically, graphene oxide (GO) membranes emerged as a promising membrane material due to the abundant oxygen-containing functional groups [29,30], adjustable interlayer spacing [31–33], and excellent mechanical strength - possessing high flexibility [34,35]. Nonetheless, GO membranes have low water permeability due to narrow interlayer spacing between GO nanoflakes and are susceptible to fouling due to the adsorption properties of the membrane and the occurrence of concentration polarization phenomenon during the filtration processes [36,37]. In addition, the GO membrane is prone to swelling in an aqueous solution which causes a deterioration of separation performance and shortened service life of the membrane [38]. Therefore, to improve the practicality of GO membranes in water separation, a mild thermal reduction is commonly used as a post-treatment method, inhibiting swelling and effectively improving the stability of the GO-based membrane [39]. Unfortunately, reduced graphene oxide (rGO) membranes normally demonstrate lower permeability and selectivity than theoretical calculations [40]. Thus, various nanoparticles (NPs) such as zinc oxide (ZnO) [41], titanium oxide (TiO_2) [42], silicon oxide (SiO_2) [43], and metal-organic frameworks (MOFs) [44–48] have been intercalated between GO nanoflakes and function as a rigid spacer between the nanochannels, enhancing the permeability of the rGO membrane.

To date, constructing membranes with self-cleaning properties via photocatalytic degradation is one of the most promising technologies for energy-efficient environmental cleaning [49]. This photo-induced self-cleanable membrane exhibits superior anti-fouling performance due to the degradation of organic dyes under UV light or visible irradiation. Semiconductor metal oxide NPs such as TiO_2 and ZnO not only act as a rigid spacer between graphene nanoflakes, but also endow the rGO membrane with photocatalytic properties [50]. Among them, ZnO has a wide bandgap (3.2 eV) and a large excitation binding energy of 60 meV. It is widely applicable for graphene oxide membrane modification due to its affordability, ease of synthesis, and lower toxicity than TiO_2 [51–53]. Li et al. obtained rGO/ZnO/PSF membranes via the phase inversion method for the removal of dye from wastewater [54]. Similarly, Al-Rawashdeh et al. fabricated GO-ZnO membranes embedded with metals such as silver (Ag) and Copper (Cu) for the removal of organic dyes via photocatalytic reaction. In each case, the as-synthesised membranes exhibit excellent photocatalytic activities with 100% removal of dyes [55]. However, ZnO nanoparticles that were embedded in the membrane might easily fall off and cause secondary pollution [56]. One way of promoting the chemical interaction between different components of a composite membrane is to synthesize the nanoparticles in the presence of GO flakes. In this work, ZnO nanoparticles were synthesised in the presence of GO flakes to take advantage of the maximum chemical bonding. Hence, the development of a cost-effective and facile approach to improving the stability and self-cleaning capability of the membranes is of great importance as well as huge interest.

In this work, we report a facile fabrication of a photocatalytic self-cleaning rGO-ZnO membrane with a unique nanostructure. The ZnO NPs intercalated in the first few layers of GO nanoflakes act as a photocatalytic self-cleaning layer and the GO layers below act as a selective layer. The performance of the membranes for each stage of fabrication and the mechanism of rejections were proposed. To determine the molecular cut-off of the membranes, different types of dye sizes were analysed for rejection performance. The membranes also exhibit excellent photocatalytic self-cleaning properties, and the self-cleaning mechanism was discussed.

2. Experimental section

2.1. Materials

Graphene oxide (GO) 1% dispersion was purchased from William Blythe. Zinc nitrate hexahydrate ($Zn(NO_3)_2{\cdot}6H_2O$; 98%), Tris-HCl buffer solutions, dopamine hydrochloride ($C_8H_{11}NO_2{\cdot}HCl$; 99%) Tris-HCl (1 M), Methylene blue ($C_8H_{11}ClN_3S$), Methyl orange ($C_{14}H_{14}N_3NaO_3S$), Rhodamine B ($C28H_{31}ClN_2O_3$), Rose bengal ($C_{20}H_4Cl_4I_4O_5$), Uniblue A ($C_{22}H_{16}N_2O_7S_2$) were obtained from Alfa Aesar. Reactive black 5 ($C_{26}H_{21}N_5Na_4O_{19}S_6$), Reactive blue 4 ($C_{23}H_{14}Cl_2N_6O_8S_2$), Direct red 80 ($C_{45}H_{26}N_{10}Na_6O_{21}S_6$), Fast green F ($C_{37}H_{34}N_2Na_2O_{10}S_3$), Trypan blue ($C_{34}H_{28}N_6O_{14}S_4$), Remazol brilliant blue R ($C_{22}H_{16}N_2Na_2O_{11}S_3$), Reactive orange 16 ($C_{20}H_{17}N_3Na_2O_{11}S_3$), Sodium hydroxide (NaOH) were obtained from Sigma Aldrich. Polyethersulfone (PES) membrane (47 mm, 0.1 μm pore size) was ordered from Sartorius.

2.2. Fabrication of polydopamine (PDA) coating membranes

PDA-coated PES membrane synthesis was conducted by dip coating the PES membrane with 100 nm pores (Sartorius) in a prepared solution of 0.1 g PDA and 50 mL HCl-Tris buffer solution (50 Mm) for 1 hour (h). After soaking, the coated membrane was washed with deionised water, removing residual unbound PDA on the surface of PES membranes. The as-prepared substrate indicated as P membrane was stored in ultrapure water.

2.3. Preparation of single-layer graphene oxide (SLGO) membranes

Monolayer graphene oxide was firstly dispersed in deionised water under vortex mixing (SciQuip Vortex Varimix) at 2400 rpm for 3 minutes (min), followed by 2 h sonication (Fisherbrand FB11002). The dispersion was then centrifuged at 8000 rpm for 1 h at 20 °C (Thermo Electron Corporation, PK131R) to remove large aggregates in the suspension. The obtained solution was used as the stock SLGO solution, the concentration of which was determined by Ultraviolet–Visible (UV–Vis) spectroscopy (Thermo Scientific Evolution 60) (See supporting information for further details, Figs. S1 and S2). Subsequently, films with predictable theoretical thicknesses were prepared by simple dilutions of the stock solution, the resultant SLGO nanoflakes were characterised by atomic force microscopy (AFM). The SLGO-coated membrane was fabricated by depositing the SLGO dispersion onto PES-PDA (P) membrane support via vacuum filtration (Millipore filtration system) forming the P-GO membrane. The actual thickness of the SLGO layer was determined by cross-sectional Scanning Electron Microscopy (SEM) analysis.

2.4. Preparation of rGO/ZnO hybrid membranes

rGO/ZnO hybrid membranes were fabricated by introducing Zn ions into the SLGO solution prior to vacuum filtration. More specifically, 150 mL of SLGO stock solution containing ~400 nm of GO was sonicated for 30 min. Subsequently, 0.2 M of $Zn(NO_3)_2{\cdot}6H_2O$ was added dropwise with vigorous stirring for 1 h at room temperature (25 °C), allowing for maximum adsorption of zinc ions to GO nanoflakes. The resultant mixture was then filtered through the P-membrane forming a P-GO/Zn^{2+} film. Saturating the film surface, the as-prepared membrane was then immersed in 0.2 M $Zn(NO_3)_2{\cdot}6H_2O$ for 2 h at room temperature. Thereafter, 0.4 M of sodium hydroxide solution was filtrated through the P-GO/Zn^{2+} membrane at 50 °C. Finally, the as-prepared membrane was subjected to heat treatment at 150 °C for 4 h to fabricate a P-rGO/ZnO membrane.

2.5. Membrane performance analysis

The membrane's filtration performance was evaluated using a

vacuum filtration apparatus (0.5 bar). The flux *(F)* of the membrane was determined by calculating the volume of permeate in unit time, according to Eq. (1):

$$F = V / (A \bullet \Delta t \bullet \Delta P) \quad \text{Eq. (1)}$$

Where V is the volume of permeate (L), A is the effective filtration area (m^2), Δt is the filtration time (h), and ΔP is the applied pressure (bar). The flux of the membrane for various organic dyes was tested by filtering 50 mL of the feed solution through the membrane. The dye concentration was measured using a UV–Vis spectrophotometer (Thermo Scientific Evolution 60). The dye rejection *(R)* was calculated according to Eq. (2):

$$R = (1 - C_p / C_f) \times 100\% \quad \text{Eq. (2)}$$

Where C_p is the dye concentration (ppm) in permeate and C_f is the dye concentration (ppm) in the feed solution.

2.6. Photocatalytic self-cleaning experiment

The photocatalytic self-cleaning property of the as-prepared P-rGO/ZnO membrane was evaluated by continuous filtration of rose bengal (RB) dye with a concentration of 10 mg/L at 0.5 bar for 2 h. The membrane was exposed to UV irradiation (Xenon UV–visible lamp) with a wavelength of 350–450 nm for 1 h and subjected to another cycle. The permeate was collected every 5, 40, and 120 min and analysed using a UV–Vis spectrophotometer (Thermo Scientific Evolution 60) to determine the membrane's long-term use capabilities.

2.7. Characterisations

The surface and cross-sectional morphology of the prepared membrane were characterised using scanning electron microscopy (SEM; JEOS JSM-ITI100). Cross-sectional imaging was conducted by freeze fracturing the membrane in liquid nitrogen prior to SEM analysis. Contact angle (CA) measurements were performed using the Ossila contact angle goniometer and software. UV–Vis spectra for analysing the dye concentrations were performed using a Thermo Scientific Evolution 60 UV–Vis spectrophotometer. XPS analysis was conducted using X-ray photoelectron spectroscopy (XPS; Scienta 300) with SPECS monochromated XPS in monochromated mode with aluminum Kα radiation. X-ray diffraction (XRD; Bruker D8 Advance) analysis was carried out with Cu Kα radiation in a 2θ range of 4.0°–40.0°. The energy dispersive X-ray analysis (EDS) analysis was performed using Oxford Instruments Xman^N 150 detector. Fourier transform infrared spectroscopy (FTIR; Nicolet iS10) analysis was carried out at 500–4000 cm^{-1}. Atomic force microscopy (AFM) images were obtained on a JPK Nanowizard 4XP under tapping mode. The heavy metal concentration before and after adsorption was measured using inductively coupled plasma optical emission spectroscopy (ICP-OES) PerkinElmer Optima 8300 DV. The material potential was measured by zeta potentiometer (Litasizer).

3. Results and discussion

3.1. Preparation and characterization of the rGO-ZnO hybrid membranes

In this study, the microporous PES membrane substrate was first coated with a thin layer of polydopamine (PDA) (see section 2.2), as shown in Fig. 1. After coating, the residual PDA on the substrate surface was removed by washing it with deionised water and the membrane was noted as a P-membrane. To complete step 1. single-layered graphene oxide (SLGO) dispersion with Zn^{2+} ions was first prepared by dropwise addition of $Zn(NO_3)_2{\cdot}6H_2O$ solution into the SLGO solution under 1 h vigorous stirring at room temperature, which was then deposited on the P-membrane via a simple vacuum filtration assembly method as reported previously [57], producing an SLGO-Zn^{2+} membrane on the surface of the P-membrane (noted as P-GO/Zn^{2+} membrane). Note that the zinc metal ions were employed as intercalation guests between GO nanoflakes, acting as spacers between the GO nanoflakes. The zinc ions can be easily incorporated into the GO nanostructure via electrostatic adsorption between the positively charged zinc metal ions and the negatively charged GO functional groups. Additionally, in the P-GO/Zn^{2+} membrane, the zinc ions can be adsorbed strongly via the cation-π interaction with the graphitic basal planes of GO, bridging

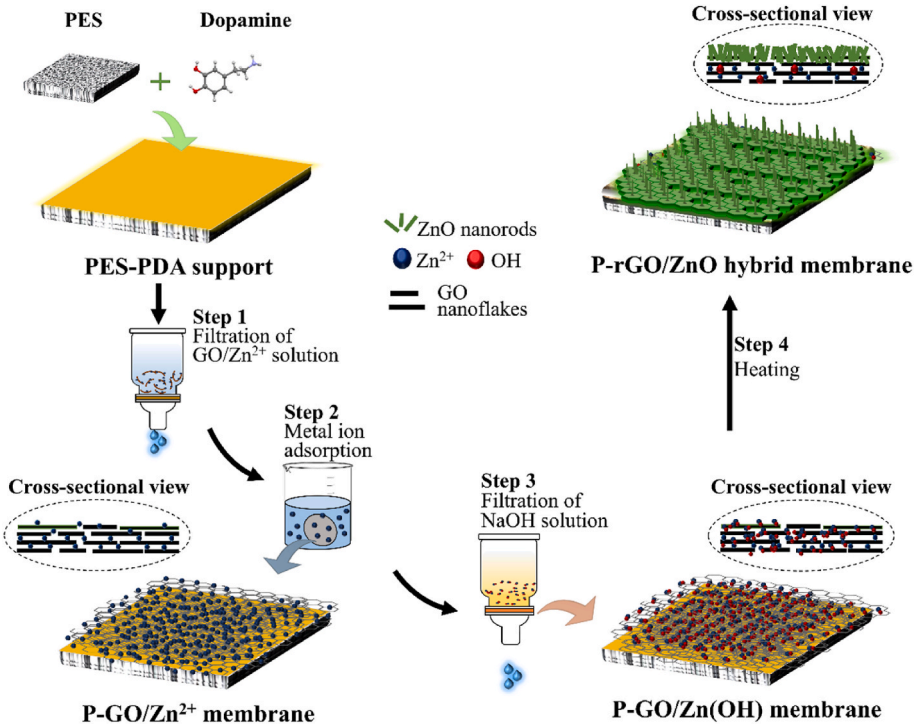

Fig. 1. Schematic diagram of the fabrication process of photocatalytic self-cleaning P-rGO/ZnO hybrid membranes.

adjacent graphene oxide nanoflakes and further enhancing the mechanical properties of GO membrane structures [57–59]. Therefore, in step 1, the zinc ions either permeate through the membrane or become intercalated, bonding between GO nanoflakes. To fully saturate the membrane structure, the as-synthesised P-GO/Zn^{2+} membrane was soaked in $Zn(NO_3)_2{\cdot}6H_2O$ solution once again. After that, a NaOH solution was filtrated through the Zn^{2+}-saturated membrane, promoting the ionic-dipolar interactions between the hydroxyl group of NaOH and the zinc ion, generating the intermediate $Zn(OH)_4^{2-}$ [60,61], and thus forming a P-GO/Zn(OH) membrane. Finally, the membrane was heated in an oven to dehydrate the $Zn(OH)_4^{2-}$ phase, forming ZnO on the membrane surface. The resulting hybrid membrane is denoted as the P-rGO/ZnO membrane [62]. It is worthwhile mentioning that the ZnO nanorods were mainly formed on the membrane surface layers serving as spacers between the GO layers and also as efficient photocatalysts for organic dye decomposition upon the exposure of UV–visible lights, endowing an interesting surface self-cleaning function to the membrane (see section 3.5 Photocatalytic self-cleaning properties and mechanism).

Surface morphology and cross-sectional of the as-synthesised membranes were characterised using SEM to understand their nanostructures at each preparation step (Fig. 2a–i and insets). As shown in Fig. 2a, the clean PES membrane exhibited a porous architecture with a pore size of 100 ± 19 nm (Fig. S3a). It is worth noting that PES has a clean, white surface (Fig. S2a). The PES underwent PDA coating at various durations (30 min, 60 min, and 90 min). From the flux and dye rejection results, it can be concluded that 1 h is effective in coating the PES membrane with PDA (Fig. S4). Following the PDA coating, the pore size was found to be slightly reduced to 80 ± 14 nm (Fig. 2b and Fig. S3b) and the white surface of the membrane became faintly tainted with a light brown colour (Fig. S2b), indicating the successful deposition of PDA coating on the PES membrane surface. It is worth noting that the pore size of these two membranes was measured using the ImageJ software. After vacuum filtration of the SLGO solution, the SEM images of the membrane surface (Fig. 2c and inset) revealed that the PDA-coated support had been uniformly covered by GO nanoflakes. The as-prepared GO membrane showed an intact and smooth surface without any visible cracks or pinholes, indicating GO nanoflakes integrated well with the PES/PDA substrate which is attributed to the high adhesion ability and excellent reactivity of the hydroxyl and amine groups on the PDA layer [63,64]. Simultaneously, oxygen functional groups of GO, such as epoxy, carboxyl, and hydroxyl groups, could react with the amine group of the polydopamine layer [65], thus forming a highly stable PDA-GO interaction. The cross-sectional views of the as-synthesised membrane revealed an ultrathin GO layer on the upper surface of the PES substrate with a thickness of 305 ± 9 nm (Fig. 2c inset). As a result of the GO/Zn^{2+} addition, the PES substrate surface became a uniform light brown colour, further suggesting the even GO coverage on the PDA-coated PES substrate (Fig. S2c). In comparison to pure GO coatings, the addition of $Zn(NO_3)_2{\cdot}6H_2O$ in the GO suspension and subsequent membrane soaking did not change the surface morphology of the resulting membrane (Fig. 2c and d). This indicated that the adsorbed Zn^{2+} ions did not cause any obvious damage to the surface as well as the layered structure of the membrane. However, cross-sectional morphology indeed revealed an obvious increase in the GO thickness from 305 ± 9 nm to 341 ± 10 nm (Fig. 2c and d insets). This might be due to abundant C–OH moieties forming as a result of the Zn ion-induced ring-opening of epoxides on the GO nanoflakes. Hence, the intercalation of zinc ions into the membrane structures facilitated by the C–OH moieties and the in-plane carbonyl group leads to an increase in the interlayer spacing [58]. After sodium hydroxide filtration, though a similar surface morphology was observed (Fig. 2e), the photograph of the P-GO/Zn(OH) membrane shows the membrane surface darkens (Fig. S2e). The change in surface colour

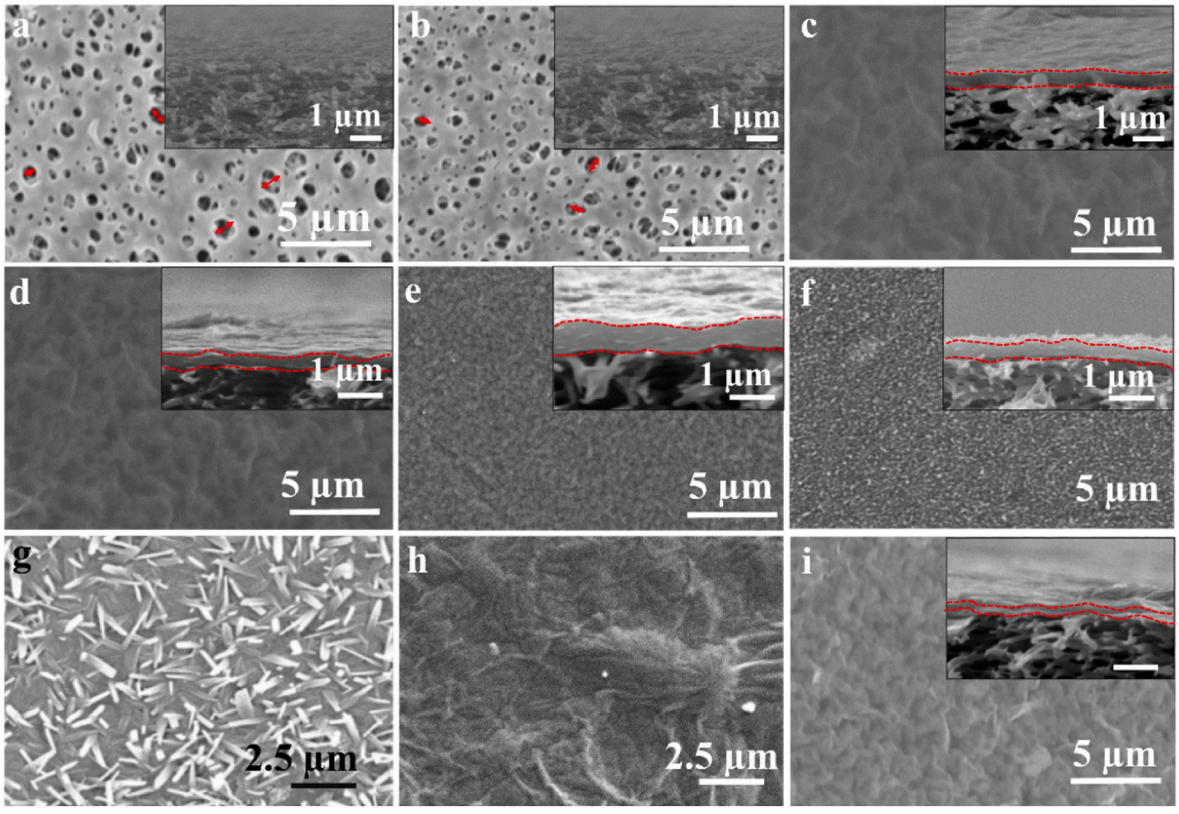

Fig. 2. SEM images (top view) of (a) PES support, (b) PES-PDA support, (c) P-GO membrane, (d) P-rGO/Zn^{2+} membrane, (e) P-rGO/$Zn(OH)_2$ membrane, (f) P-rGO/ZnO membrane, (g) P-rGO/ZnO membrane at higher magnification, (h) the backside of P-rGO/ZnO peel-off membrane at higher magnification, and (i) P-rGO membrane. The insets are corresponding cross-sectional SEM images. Red arrows in (a) and (b) denote the pore size of the substrates. Red dashed line pairs indicate the membrane thickness. (For interpretation of the references to colour in this figure legend, the reader is referred to the Web version of this article.)

indicated the oxidation of zinc ions upon the addition of hydroxide ions. Furthermore, the cross-sectional analysis highlights a significant increase in membrane thickness to 408 ± 12 nm. This is because the Zn^{2+} ions reacted with hydroxide ions (OH^-) forming $Zn(OH)_2$ (Eq. (3)) and with the excess of OH^-, a large quantity of $Zn(OH)_4^{2-}$ ions were produced (Eq. (4)), thus, causing the expansion of the interlayer spacing [66,67].

$$Zn^{2+} + 2\ OH^- \rightarrow Zn(OH)_2 \quad \text{Eq. (3)}$$

$$Zn(OH)_2 + 2\ OH^- \rightarrow Zn(OH)_4^{2-} \quad \text{Eq. (4)}$$

$$Zn(OH)_4^{2-} \xrightarrow[\Delta]{} ZnO + 2H_2O + 2OH^- \quad \text{Eq. (5)}$$

After the following fast heat treatment, the membrane surface turned black immediately (Fig. S2f). Fig. 2f and g showed that the membrane surface was uniformly decorated by large amounts of nanorods. According to Eq. (5), upon heat treatment of $Zn(OH)_4^{2-}$, a pure ZnO phase can be formed, hence the nanocrystals formed on the membrane surface are pure ZnO nanorods (50 ± 11.2 nm). It is worth noting that this crystal formation on the surface of the membrane was unique and was observed only on the front side region of the P-rGO/ZnO membrane. Fig. 2g reveals that ZnO nanorods formed as a result of the *in situ* crystallization were uniformly distributed over the entire upper surface of the graphene oxide membrane. Comparatively, by peeling the membrane from the PES support, the bottom side of the P-rGO/ZnO membrane exhibited a flat, smooth surface without any ZnO crystals (Fig. 2h). Therefore, it is suggested that the ZnO nanorods were mainly intercalated in the upper layers of reduced graphene oxide membrane. Interestingly, the membrane cross-section showed a significant reduction in membrane thickness to 324 nm ± 9 nm, which is comparable to that of the cross-section of the initial pure rGO membrane as aforementioned. As a control, SEM analysis was also done for pure reduced graphene oxide (rGO) membranes after similar heat treatment. As shown in Fig. 2i, abundant wrinkles were observed on the membrane surface after the reduction of GO nanoflakes [66]. The cross-sectional SEM image of the heat-treated GO membrane showed a reduced thickness of 276 ± 8 nm (Fig. 2i inset) which is ~50 nm thinner than our P-rGO/ZnO membrane. This result further confirmed that the ZnO nanorods were mainly intercalated in the top few layers of reduced graphene oxide membrane, while the majority of the structure underneath remained similar to that of pure rGO membranes in terms of thickness (See Fig. S5 for full membrane thickness analysis). Surface analysis of the membranes at each fabrication step was further assessed using AFM to observe changes in surface roughness (Figs. S6a–d). In the initial analysis, the P-rGO membrane displayed a surface roughness characterised by a root mean square (Sq) value of 72.96 nm. After the incorporation of Zn, the P-rGO/Zn membrane exhibited a slight decrease in surface roughness to 67.36 nm, suggesting a smoother surface, as corroborated by SEM observations. Conversely, the P-GO/ZnOH membrane displayed a higher surface roughness of 105.4 nm. Notably, the P-rGO/ZnO membrane demonstrated the highest surface roughness of 214.6 nm, owing to the existence of ZnO nanorods. The alteration of the surface roughness of the membranes revealed by AFM analysis is in agreement with the previous SEM observation.

3.2. Chemical and physical properties of the as-synthesised membranes

Underpinning the chemical composition of the as-synthesised

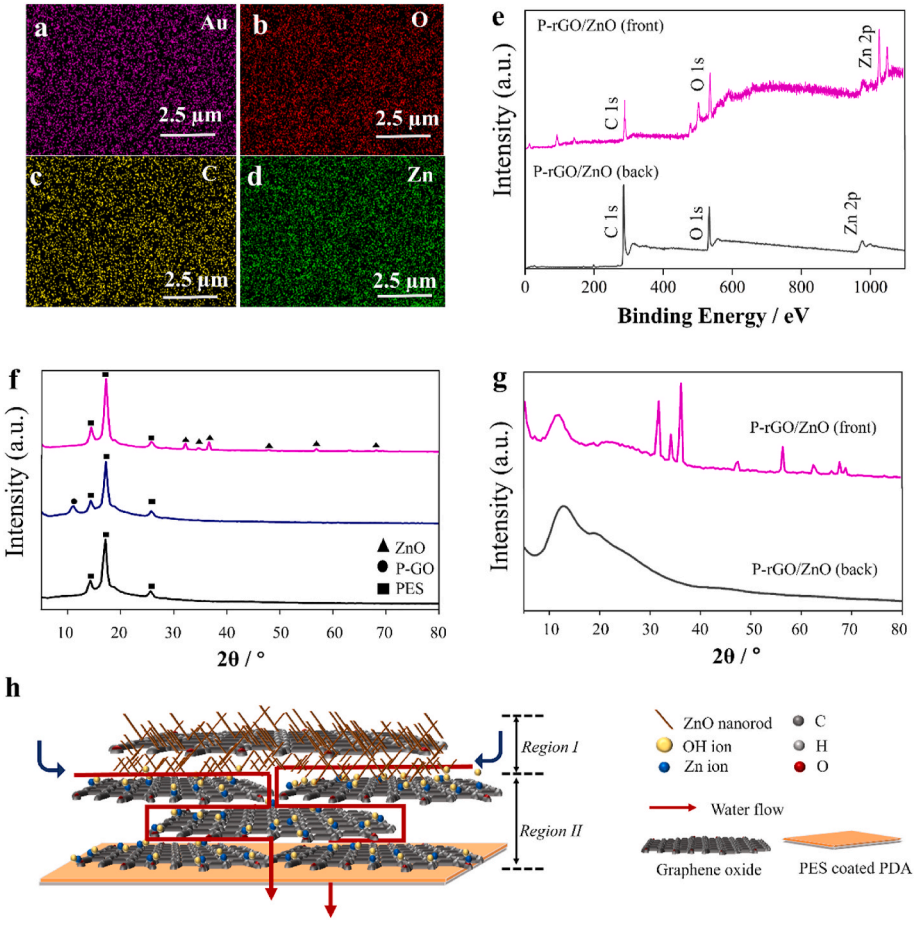

Fig. 3. (a–d) EDS mapping of Au, O, C, and Zn; (e) XPS wide scan of the peel-off P-rGO/ZnO membrane front and back sides; (f) XRD spectrum of PES, P-GO, and P-rGO/ZnO membrane; (g) XRD spectrum of front and back sides of peel-off rGO-ZnO membrane; and (h) schematic illustration of P-rGO/ZnO membrane structure.

membranes, SEM-EDX mapping was first conducted for the P-rGO/ZnO membrane surface. Carbon (C), oxygen (O), and zinc (Zn) elements were analysed to show the distribution and presence of ZnO on the P-rGO membrane (Fig. 3a–d). It was observed that the Zn and O elements were distributed uniformly on the membrane surface, indicating the successful *in situ* synthesis of ZnO on the rGO surface. In addition, the presence of different chemical groups of the hybrid membrane surface was studied using XPS analysis. The wide scan of the P-rGO/ZnO membrane surface revealed four binding energy peaks at 287.4 eV, 532.4 eV, 1024.5 eV, and 1022.7 eV, corresponding to carbon (C 1s), Oxygen (O 1s), zinc (Zn $2p_{3/2}$), and zinc (Zn $2p_{1/2}$), respectively (Fig. 3e), suggesting that ZnO is successfully synthesised on the GO membrane [68]. The high-resolution scans of the elements for the front and back side of the rGO/ZnO membrane were shown in Fig. S7. XPS analysis showed the surface of P-rGO/ZnO was composed of 19.9% carbon, 32.1% oxygen, and 44.3% zinc. This large difference in zinc and carbon can be attributed to the dense, uniform coverage of ZnO on the surface of the rGO membrane. As expected, XPS analysis of the backside of the membrane showed a trace amount of Zn but mainly rGO structures with a composition of 60.9% carbon, 39.0% oxygen and 0.1% Zn, which again confirmed that the pure ZnO nanophase was only present on the top membrane layers. To monitor the change in membrane structure, XRD analysis was also conducted on membranes after each synthesis step and the peel-off rGO/ZnO membrane (Fig. 3f and g). As shown in Fig. 3f, clean PES supports showed 3 peaks (marked with solid squares) at 2θ angles of 25.7°, 17.2°, and 14.3°, which were visible in each spectrum. After GO coating, the XRD pattern showed an additional peak at 11.1°, indicating a thin layer of single-layered graphene oxide (SLGO) covering the surface of the PES membrane. Comparatively, the final P-rGO/ZnO membrane exhibited significantly more peaks on the XRD spectra. More specifically, peaks were observed at 31.7°, 34.3°, 36.2°, 47.5°, 56.5°, 65.1°, and 69.1°, representative of [100], [002], [101], [102], [110], [103], and [112] planes, respectively. According to the previous reports, these peaks are the characteristic diffraction peaks of a pure ZnO phase [69]. Interestingly, the peak previously attributed to GO (11.1°) is not visible in this spectra. This is due the dense coverage of ZnO nanorods on the membrane surface and also the reduction of the GO, forming rGO (Fig. S8).

To further confirm the presence of the ZnO phase in the membrane structure, the XRD analysis was conducted on both the front side and back side of the peel-off P-rGO/ZnO membrane (Fig. 3g). The front side exhibited intense peaks of ZnO as discussed above [69]. Comparatively, the back side of the hybrid membrane did not show typical ZnO characteristic peaks.

Based on the above results, the configuration of the as-synthesised P-rGO/ZnO membrane was thus proposed and shown in the schematic diagram Fig. 3h. Briefly, this new and simple *in situ* crystallization process promoted the formation of asymmetric nanostructures in the membrane, composed of two regions. In region I, the ZnO nanoparticles and zinc ions are intercalated into the top few GO layers, leading to the enlargement of the interlayer spacing of GO and acting as the functional photocatalytic layer for cyclic membrane regeneration. In contrast, underneath the upper layers – region II, the pre-adsorbed zinc ions react with a significantly reduced concentration of sodium hydroxide solution forming a trace of normal Zn hydrates due to the lack of NaOH [57]. These intercalating materials (ZnO nanorods and Zn hydrates) co-exist and act as spacers between the rGO nanoflakes, preventing the shrinkage of the nanochannels during heat treatment, and hence forming a hybrid, selective membrane structure for small molecule filtration. With expanded nanochannels in the rGO layers and effective intercalated spacers, the P-rGO/ZnO membranes were tested for small organic molecular filtration (e.g., dye molecules). Their separation performance and UV–visible light-stimulated photocatalytic self-cleaning function for cyclic membrane regeneration were also studied in detail.

3.3. Membrane separation performance

As aforementioned, water purification is in high global demand owing to the rapid increase in population. An energy/cost-effective method of achieving this is membrane separation which holds a lower carbon footprint than conventional methods currently employed in the industry [70]. In this work, the photocatalytic self-cleaning P-rGO/ZnO membranes were used to separate small dye molecules with different molecular sizes and charges. The wetting properties of the fabricated membranes were first studied by measuring the surface static water contact angles of the prepared membranes. As presented in Fig. 4a, the contact angle decreased from 45° ± 2° for pristine PES membrane to 39° ± 7° for PDA/PES membrane, implying a more hydrophilic surface formed due to the abundance of hydrophilic amine groups of PDA. The water contact angle further decreased to 35° ± 3° after filtration of the GO solution. This can be attributed to the existence of hydrophilic groups of GO nanoflakes. Interestingly, after GO/Zn^{2+} deposition, the contact angle increased to 54° ± 6° for the newly formed P-GO/Zn^{2+} membrane. The increase in the membrane hydrophobicity is due to the ion exchange between zinc ions and protons (H^+) on the oxygen functionalities of the GO nanoflakes [58]. Comparatively, the contact angle value of P-GO/$Zn(OH)_2$ significantly reduces to 19° ± 2°. This advantageous hydrophilicity is attributed to the presence of the hydrophilic hydroxyl groups interacting with the zinc ions on the surface of the GO membrane. Interestingly, after the heat treatment, the membrane surface remained hydrophilic with a low water contact angle of 20° ± 2°. It is completely different to the conventional rGO membranes which are usually much more hydrophobic (78° ± 5°). The existence of ZnO not only optimised membrane surface structure but also endowed the membrane with beneficial hydrophilicity [71,72].

To study the influence of membrane chemical structure on the separation performance, a systematic study using aqueous rose bengal (RB) solution (10 ppm) was conducted on the as-synthesised membranes at each stage of the fabrication (Fig. 4b), and their corresponding separation mechanism was proposed accordingly (Fig. 4c). As shown in Fig. 4b, the pure GO membrane has a water flux of 73 ± 3.2 L m^{-2} h^{-1} bar^{-1} with an RB rejection of 97 ± 4.9%. After simply depositing a fixed amount of GO nanoflakes (~305 nm) on the PES/PDA support, the P-GO membrane exhibited a higher water flux of 138 ± 6.9 L m^{-2} h^{-1} bar^{-1} with an RB rejection of 98 ± 4.9%. The increase in water permeance is attributed to the presence of PDA which helps with the adhesion and subsequent deposition of GO nanoflakes to the porous PES substrate, forming GO membrane with a more selective structure and also reducing the chance of PES pore blockage during the filtration of GO nanoflakes [73,74]. After the intercalation of Zn^{2+}, the water permeance for the P-GO/Zn^{2+} membrane further increased to 238 ± 11 L m^{-2} h^{-1} bar^{-1}. This is owing to the expansion of interlayer spacing as a result of Zn^{2+} adsorption. The adsorption of Zn^{2+} on the GO nanoflakes is a result of the strong surface complexation with oxygen functionalities [75]. Despite the enhancement in water permeation, the membrane dye rejection was decreased to 92 ± 4.6%, indicating that the intercalated Zn^{2+} showed no apparent gating effect on the permeance of RB [57]. Upon the addition of NaOH through the P-GO/Zn^{2+} membrane, Zn $(OH)_4^{2-}$ ions are formed between the GO membrane interlayers. Consequently, the water permeance was significantly increased to 628 ± 31 L m^{-2} h^{-1} bar^{-1} with a further decrease in dye rejection to 75 ± 3.75%. After heat treatment, $Zn(OH)_4^{2-}$ was transformed into ZnO nanorods on the membrane surface. In the meantime, GO nanoflakes were mildly reduced to the rGO membrane, forming a P-rGO/ZnO membrane as discussed in the above section. Interestingly, the P-rGO/ZnO membrane only showed a slight decrease of water flux to 400 ± 21 L m^{-2} h^{-1} bar^{-1} but with a significantly increased RB rejection rate of up to 98.8 ± 1.2%. According to previous studies, conventional rGO membranes with a similar thickness of ~300 nm have a significantly lower flux of ~40 L m^{-2} h^{-1} bar^{-1} [76,77]. However, the P-rGO/ZnO membranes fabricated in this work showed ten times higher water flux, while achieving a

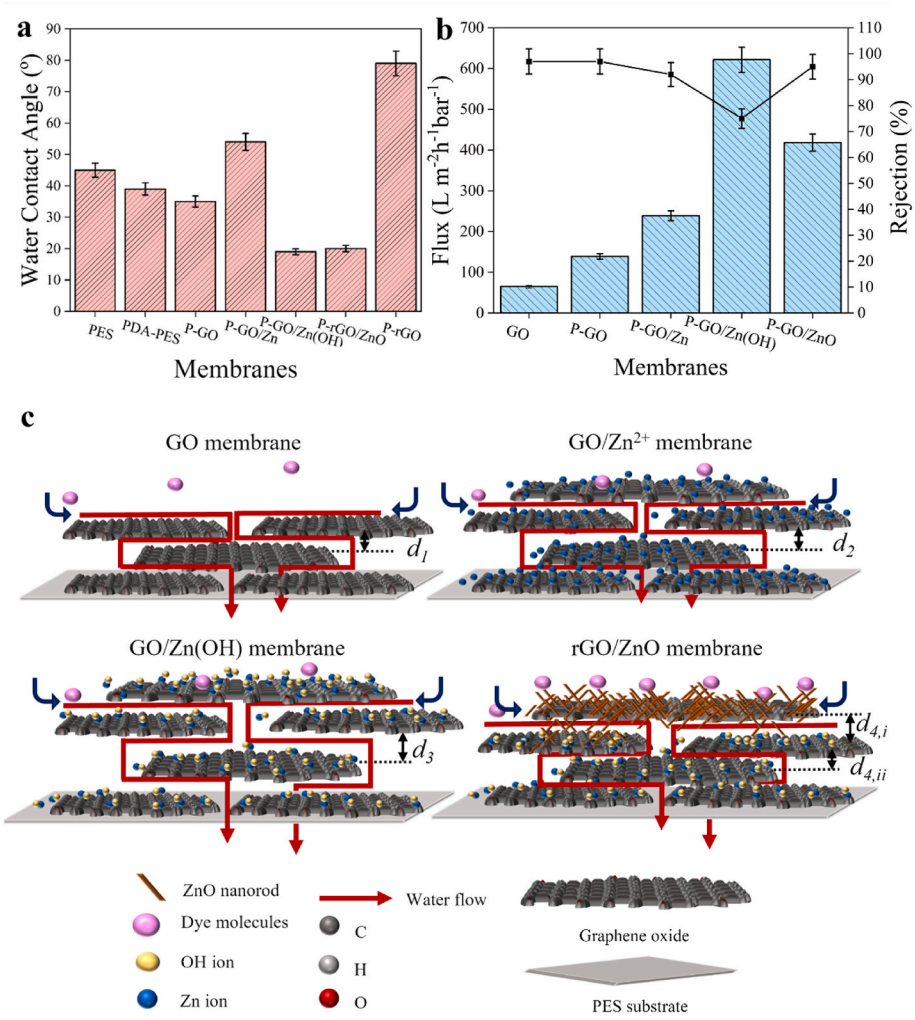

Fig. 4. (a) Water contact angles of as-synthesis membranes. (b) Rose bengal (RB) permeance and rejection of the as-synthesis membranes. (c) Schematic interpretation of the membrane structure and possible molecule transport mechanism of the GO membrane, GO/Zn^{2+} membrane, GO/Zn(OH) membrane, and rGO/ZnO membrane.

satisfactory RB rejection rate of >98%, This is owing to the unique hybrid membrane structure formed using the combined GO self-assembly and in-situ ZnO crystallization method. In this work, the membrane's dye separation efficiency was evaluated by analyzing the concentration change of RB in the feed and permeate using UV–Vis spectroscopy. Generally, the UV–vis spectra of the filtrate showed a general decrease in dye concentration, however, each membrane exhibited varying separation efficiencies (Fig. 4b and Fig. S9).

Based on the membrane performance and their XRD, SEM, XPS and EDX characterization results, potential separation mechanisms of the as-synthesised membranes before and after *in-situ* crystallization of ZnO nanoparticles were proposed and schematically illustrated in Fig. 4c. In the pure GO membrane, there are typically two forms of diffusional channels for water permeation. Firstly, vertical nanochannels are formed by in-plane nanosized defects/pores and gaps formed between the edges of neighbouring GO nanoflakes. Secondly, horizontal nanochannels, which are also known as interlayer spacing (d_1), are the interspacing between GO layers. Hence, numerous molecular diffusion pathways are formed from the interconnection between these nanochannels [78]. In molecular separations, to achieve good selectivity, the interlayer spacing (d_1), defects on the GO basal plane, and nanogaps between GO nanoflakes must be small enough to reject undesired molecules. Therefore, an increase in nanochannel size may lead to higher molecular diffusion but sacrifice the rejection rate. In this case, size exclusion appears as the dominant separation mechanism for the transport of molecules in a lamellar GO membrane, with separations mainly dependent on the size and length of these structural nanochannels. In our study, horizontal nanochannels (or interlayer spacing) played a vital role in controlling both water flux and separation efficiency. More specifically, the alteration of intercalating materials allows for the effective control of spacing between the GO nanoflakes. For example, in the case of P-GO/Zn^{2+}, an increase in permeation rate to 238 ± 11 L m^{-2} h^{-1} bar^{-1} whilst a decrease in rejection rate to 92 ± 4.6% was observed [75]. This is attributed to the excessive zinc ions intercalation between the interlayer capillaries, which increases the interlayer spacing (d_2). Hence, the water transport rate was higher than that of the GO membrane, while the RB rejection rate was reduced. In the P-GO/Zn(OH) membrane, the reaction between the pre-adsorbed Zn^{2+} ions and NaOH led to the formation of $Zn(OH)_4^{2-}$, resulting in the further expansion of the nanochannels. Therefore, an enlarged interlayer spacing (d_3) was formed leading to a significant increase in the water flux to 628 ± 31 L m^{-2} h^{-1} bar^{-1}, however, accompanied by a decrease in the rejection rate to 75 ± 3.75%. In the last preparation of the P-rGO/ZnO membrane, a fast heat treatment (150 °C for 4 h) was applied to transfer pre-formed $Zn(OH)_4^{2-}$ to the ZnO phase and in the meantime to reduce GO to rGO, forming a unique hybrid membrane structure with superior molecular sieving abilities. The ZnO nanorods formed in the top layers of GO ("region 1") act as spacers for fast water

permeation as well as a pre-screening molecular sieve layer (during membrane regeneration) for photocatalytic dye molecule removal upon exposure under UV lights. The analysis of zeta potential indicates that the surface of the P–rGO/ZnO membrane carries a negative charge (Fig. S11). Hence, the negatively charged membrane surface ("region I″ with an interlayer spacing of *d4i*) selectively adsorbs and rejects dye molecules via electrostatic attractions and repulsions [76]. Comparatively, lower regions of the P–rGO/ZnO membranes ("region II") have a reduced interlayer spacing (*d4ii*) similar to that of pure rGO membranes and act as a selective molecular sieving layer for molecule distinguishing and retention based on size exclusion. It's worthwhile mentioning that the pre-adsorbed zinc ions in this region may not be able to form ZnO as suggested by the above XPS, XRD and SEM results due to the lack of NaOH during the hot filtration process. Thus, the overall membrane thickness (~324 nm) after fast heat treatment remained quite comparable to that of the initial GO membrane without Zn ions and $Zn(OH)_4^{2-}$ (~305 nm), though the top membrane layer has full coverage of ZnO nanorods. As a result, these P–ZnO/rGO membranes exhibited an enhanced water transport rate (400 ± 21 L m^{-2} h^{-1} bar^{-1}) and high retention of dye molecules (98.5 ± 1.2%). Furthermore, an additional analysis of the permeate was conducted to detect heavy metals using ICP-OES. The results showed negligible presence of zinc, indicating no metal leaching. This underscores the strong attachment of ZnO on the rGO surface.

To further explore the separation performance and mechanism of the final P–rGO/ZnO hybrid membranes, twelve types of dyes with different sizes and charges were studied. i.e., fast green F (FCF), direct red 80 (DR-80), methylene blue (MB), methyl orange (MO), reactive orange 16 (RO-16), trypan blue (TB), rose bengal (RB), rhodamine B (RhB), remazol brilliant blue R (RBB-R), reactive black 5 (RB-5), reactive blue 4 (RB-4), uniblue A (UA). The molecular structure and different charge properties of the tested dyes are presented in Fig. S10 and Table S1, respectively. As shown in Fig. 5a, the P-rGO/ZnO membrane exhibited a consistent water flux of 400 ± 21 L m^{-2} h^{-1} bar^{-1} regardless of the dye type. However, the rejection rate of the dyes varied significantly, from 98 ± 2.9% to 60 ± 1.8% for DR-80 and MB, respectively. This can be attributed to the molecular weight variation between the dyes [79]. According to the separation results, P–rGO/ZnO membranes showed excellent separation efficiency (>96%) for dyes with high molecular weights (>800 g mol^{-1} or Da) (Fig. 5b). While for dyes with lower molecular weights (<500 g mol^{-1} or Da), poor separation rates (<80%) were obtained (Fig. 5c) (see Fig. S12 for all UV–vis results), which indicated that the membrane withholds a cut-off molecular size of ~500 g mol^{-1}. More interestingly, the dye separation efficiency of the membrane was not influenced by their negative or positive charges, further indicating the membrane's molecular sieving capability. For example, Fig. 5b shows that positive dyes (highlighted with green colour) and negative dyes (highlighted with blue colour) were rejected by the P–rGO/ZnO membrane mainly following the size exclusion mechanism. Despite the type of charge, the dye rejection rate increased as the molecular weight increased. More specifically, large molecular weight dyes such as DR-80 (1373 Da), RB (1018 Da), RB-5 (992 Da), TB (961 Da), FCF (808 Da), RB 4 (637 Da), RBB R (626 Da), RO 16 (617 Da) and UA (506 Da) exhibited a rejection rate of 98 ± 2.9%, 96 ± 2.9%, 97 ± 2.9%, 96 ± 2.8%, 96 ± 2.8% 95 ± 2.9%, 91 ± 2.7%, 90 ± 2.7% and 89 ± 2.6% respectively. The rejection rate was significantly decreased to 75 ± 1.2%, 65 ± 1.8% % and 60 ± 2.4% for RhB (479 Da), MO (327 Da) and MB (320 Da), respectively, demonstrating a direct correlation between the membrane rejection efficiency and the dye molecular weight. Hence, the dye rejection mechanism was closely associated with the steric effect, which is greatly influenced by molecular weight, size, shape and the Donnan exclusion effect [36,37]. The dye rejection over a 1500-min duration reveals that the membrane consistently maintained stable rejection at ~85% for Rose Bengal (RB), Direct Red 80 (DR 80), and RB-5 (Fig. S13). Overall, the membranes achieved the highest rejection and flux compared to the previous studies shown in Table S2.

To study whether the as-synthesised P–rGO/ZnO membrane has the capability of separating molecules based on another common type of mechanism – adsorption, the membranes were soaked in a series of dye

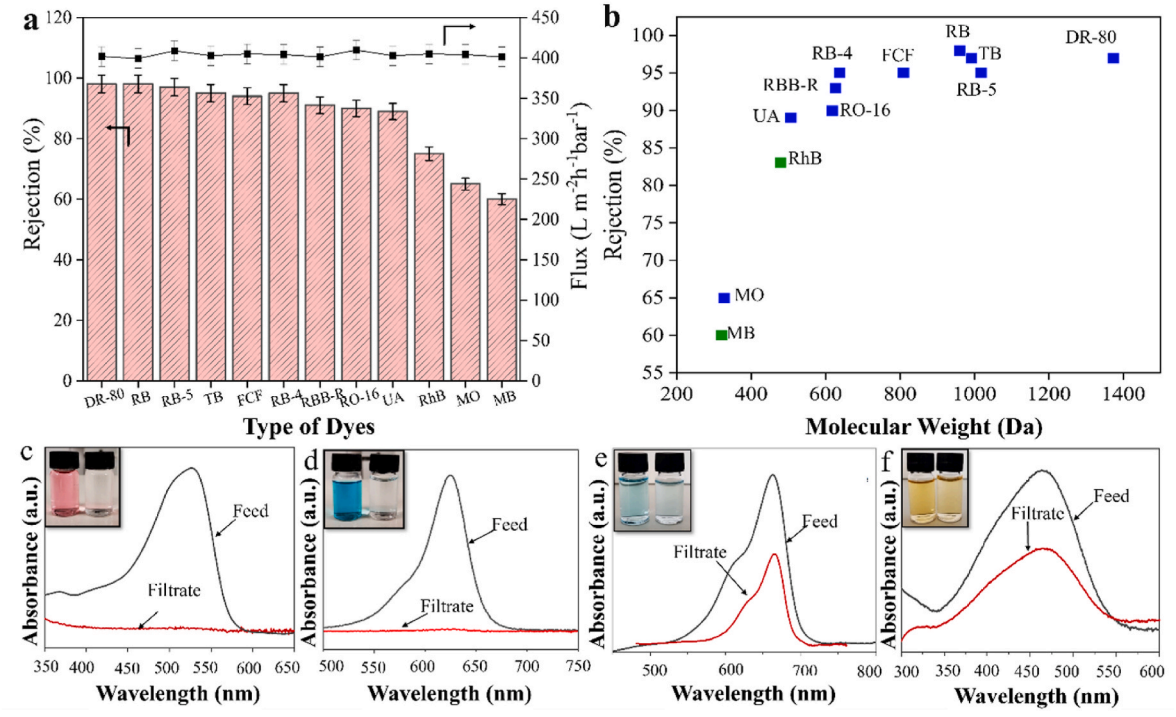

Fig. 5. (a) Permeance and rejection of the P-rGO/ZnO membrane for different types of dyes. (b) Rejection of different dyes as a function of molecular weight. UV–Vis spectra and photos (insets) of the feeds and filtrates for (c) Direct red-80 (DR-80), (d) Fast green-F (FCF), (e) Methylene blue (MB), and (f) Methyl-orange (MO). (For interpretation of the references to colour in this figure legend, the reader is referred to the Web version of this article.)

solutions with a fixed volume of 30 mL and a concentration of 50 mg L^{-1} for 12 h. The adsorption properties of the membrane toward different types of dye molecules (FCF, DR-80, RB, UA, RO 16, and RBB R) were then studied in detail. The concentration of the dye remaining in the solution after the adsorption was determined by UV–vis measurement (Fig. S14). Note that the reduction of dye concentration indicated the quantity of dye adsorbed on the membrane surface with full coverage of ZnO nanorods. Based on the adsorption results, the concentration of dyes in the final solution was reduced by 18 ± 1.2%, 21 ± 1.5%, 20 ± 2.5%, 20 ± 1.7%, 35 ± 3.2%, and 45 ± 5.1% for DR-80, FCF, RO 16, RB, UA, and RBB R, respectively. The negatively charged dyes DR-80, FCF, UA, and MO have lower reductions compared to positively charged dyes RhB and MB, which suggests that the Donnan exclusion mechanism played a minor role in the separation of dyes. The ZnO nanorods on top of rGO membrane layers have a slightly negative charge in the aqueous solution due to a reversible surface hydrolysis [80]. The interaction between the charges of dyes and the membrane surface leads to an electrostatic interaction between the dyes and the membrane surface [81], which eventually causes the physical adsorption of the dyes on the membrane surface. Lower adsorption of negatively charged dyes was, therefore, because of the repulsive interaction that existed between the anion molecules and the negatively charged ZnO nanorods based on the Donan exclusion effect, resulting in the negative charge dyes being repelled from the surface of the membrane.

3.4. Chemical and physical stability tests

Besides separation efficiency and flux, hydro-chemical stability and recyclability of the membranes are important factors in evaluating the long-term liquid separation performance. In most previous studies, rGO membranes have shown remarkable stability in both acid and alkali environments meanwhile ZnO shows only good stability in alkaline solution [82–85]. The decomposition of ZnO in aqueous solutions can be proposed as the following reactions [86,87]. To analyse the chemical stability, the P-rGO/ZnO membranes were soaked in an aqueous solution with a wide range of pH environments, pH = 3, 4, 6, 7, 9, and 11 over 7 days, and then dried and analysed by SEM and XRD (Fig. 6). As shown in Fig. 6a, the exposure to acidic conditions (pH = 6) resulted in a high degree of ZnO dissolution, attributed to the reaction of protons (H^+) with the ZnO nanorods, forming $ZnOH^+$ and H_2O and the release of zinc ions (Eqs (6) and (7)) [88]. Further lowering the pH (pH = 3 and pH = 4) showed complete dissolution of ZnO after 7 days of soaking (Fig. S15). Comparatively, as the pH increased from 7 to 11, the ZnO nanorods remained mostly intact on the surface (Fig. 6b–d). Although at pH = 9.0 and higher, mild dissolution of ZnO nanorods may occur to form the hydroxyl complexes, according to Eqs. (8) and (9). The hydroxyl complexes are known to be formed on the surface of the crystals and result in minor dissolution.

$$ZnO_{(s)} + 2H^+ \rightarrow Zn^{2+} + H_2O \quad \text{Eq. (6)}$$

$$ZnO_{(s)} + H^+ \rightarrow ZnOH^+ \quad \text{Eq. (7)}$$

$$ZnO_{(s)} + OH^- + H_2O \rightarrow Zn(OH)_3^- \quad \text{Eq. (8)}$$

$$ZnO_{(s)} + 2OH^- + H_2O \rightarrow Zn(OH)_4^{2-} \quad \text{Eq. (9)}$$

Based on our results, the P-rGO/ZnO membranes were more stable under alkaline conditions as compared to acidic conditions. The surface of the membrane maintained the dark brown colour at higher pH environments while at lower pHs the surface turned into a light brown colour (Fig. 6a–d insets). Although the SEM images showed the dissolution of ZnO nanorods at lower pHs, the rGO membrane remained intact layered structures over a wide range of pH values. This could be attributed to the PDA layer which served as a bioadhesive to strongly bind the GO nanoflakes onto the PES support, as previously discussed. In addition, the fast reduction of graphene oxide promoted the π-π conjugation between the GO layers, endowing the membranes with strong mechanical and chemical stability in the acid and alkali environments [89]. The XRD analysis of the soaked membranes showed a significant reduction in ZnO peaks after 7-day soaking at pH = 6, while the ZnO peaks remained mostly unchanged at pH > 7 (Fig. 6e).

To further understand the effect of stability on the long-term separation performance, dye separations were conducted on the P-rGO/ZnO membranes after chemical exposure. As shown in Fig. 6f, the membrane showed different reductions in water flux after soaking at different pH conditions for 7 days. After 7-day soaking at pH = 7 to 11, the membrane showed a negligible degradation in water flux (400 ± 21 L m^{-2} h^{-1} bar^{-1} to 350 ± 17 L m^{-2} h^{-1} bar^{-1}). However, the reduction of water flux (282 ± 21 L m^{-2} h^{-1} bar^{-1}) was more significant after acid soaking at pH = 6. Such lower flux may related to the dissolution of ZnO nanospacers in the rGO membrane, reducing the membrane interlayer spacing and thus water permeability. However, all membranes still maintained a high rejection of RB up to 95 ± 1.6%, 92 ± 2.3%, 97 ± 1.8%, and 95 ± 3.4% after soaking at pH = 6, 7, 9, and 11, respectively. Furthermore, the membrane exhibited good mechanical stability,

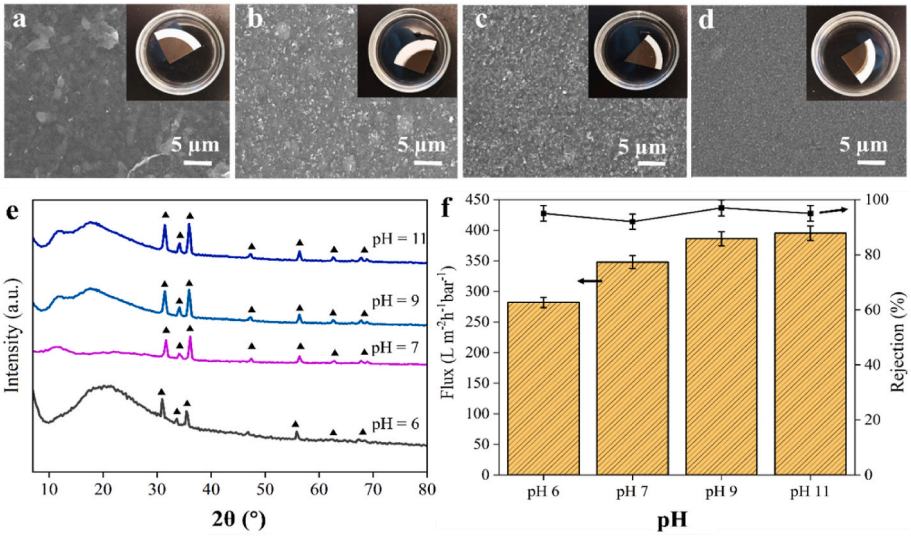

Fig. 6. SEM images of P-rGO/ZnO membranes after soaking at different pH for 7 days: (a) pH = 6, (b) pH = 7, (c) pH = 9, and (d) pH = 11. (e) XRD of membranes treated at different pHs. (f) Flux and rejection of rose bengal after soaking at different pH for 7 days. ▲ denotes characteristic ZnO diffraction peaks.

remaining intact even after undergoing 1 h of sonication (Fig. S16). The above results underscore the potential of our P-rGO/ZnO membranes operating under very harsh conditions.

3.5. Photocatalytic regeneration for cyclic membrane separation

Thanks to the hybrid membrane structure and the presence of surface ZnO nanorods, the membrane showed promising self-cleaning behaviour via photocatalytic regeneration. In the following study, the photocatalytic self-cleaning property of the P-rGO/ZnO membrane was evaluated using UV–visible light irradiation. After an RB rejection test with an initial concentration of 10 mg/L, a UV light with 365–450 nm wavelength was applied to irradiate the membrane for 1 h. Fig. 7a showed that the membrane flux was decreased continuously and eventually stabilized at ~50% of its original value at 120 min due to the adsorption of RB on the membrane surface and the likely blockage of water pathways. After only 1 h of UV radiation/regeneration, the initial water flux of the membrane was almost fully recovered. According to our results, up to 95–99% of the original flux can be restored for the next run, achieving an excellent cyclic dye separation performance. In the meantime, the rejection rate of the membrane was monitored by analysing the concentration of permeance for each cycle. The initial concentration of the permeance is shown in Fig. 7b and the UV–Vis spectra of the RB dye concentration at different times for each cycle are shown in Figs. S17a–d. The membrane exhibited an initial rejection of 96 ± 2.94%. This is because the negatively charged rose bengal dyes were mainly influenced by size exclusion due to the high molecular weight of the dyes and the adsorption mechanism that attracted dyes on the membrane surface. However, the membrane exhibited a rejection of 85 ± 10% and 77 ± 15% at 40 min and 120 min, respectively (Fig. S17e). This is due to the rejection mechanism being contributed mainly by size selection. The photocatalytic performance of the P-rGO/ZnO membrane was assessed under UV light irradiation. The findings demonstrated that, under UV irradiation, the membrane consistently sustained a flux of approximately ~400 ± 21 L m^{-2} h^{-1} bar^{-1}, coupled with rejection rates exceeding 98% (refer to Fig. S18). Moreover, the membrane's ability to recover its morphology after UV radiation underscores its self-cleaning potential. These results underscore the membrane's exceptional photocatalytic capabilities (Fig. S19).

As discussed previously, the existence of ZnO nanorods on the membrane surface exhibits considerable potential for photocatalytic properties which enhance the degradation of dyes on the membrane surface, thus leading to recovery of membrane performance. ZnO is a well-known semiconductor material, that possesses a wide range of band gap of approximately 3.37 eV [90]. Additionally, ZnO serves as a general electron-hole pair, while rGO acts as the carrier pathway. Therefore, when the P-rGO/ZnO membrane, that was synthesised as mentioned, is illuminated under UV irradiation, the electrons within the valence bands (VB) of ZnO become excited and elevated to the conduction bands (CB). This has resulted in the presence of holes (h^+) in the VB, as shown in Equation (10) [91]. Subsequently, these photogenerated electrons (e^-) in the CB can readily migrate easily to the nearest surface of rGO.

The photogenerated electrons then react with oxygen to generate superoxide radicals (Eq. (11)) which further react with H^+ to generate the first HO_2• radicals. Hydrogen peroxide molecules are formed once the HO_2• radicals come in contact with H^+ (Eq. (12)). The newly formed hydrogen peroxide molecules could further prompt the production of additional hydroxyl radicals in the presence of abundant photogenerated electrons (Eq. (13)). Whereas the empty holes formed previously then react with water (Eq. (14)) and hydroxide ions (Eq. (15)) to form photogenerated hydroxyl radicals [91,92], which are useful for decompositing organic pollutants such as dyes via an oxidation process (Eqs. (16) and (17)). The photocatalytic dye decomposition mechanism of the P-rGO/ZnO membrane is shown in Fig. 7c. All steps that are involved in the photocatalytic dye decomposition are summarised below [90,93]:

$$\text{Photons } (h\nu) + \text{ZnO} \rightarrow h^+(\text{VB}) + e^-(\text{CB}) \quad \text{Eq. 10}$$

$$e^- + O_2 \rightarrow \bullet O_2^- \quad \text{Eq. 11}$$

$$\bullet O_2^- + H^+ \rightarrow HO_2\bullet;\ HO_2\bullet + H^+ + e^- \rightarrow H_2O_2 \quad \text{Eq. 12}$$

$$e^- + H_2O_2 \rightarrow \bullet OH + OH^- \quad \text{Eq. 13}$$

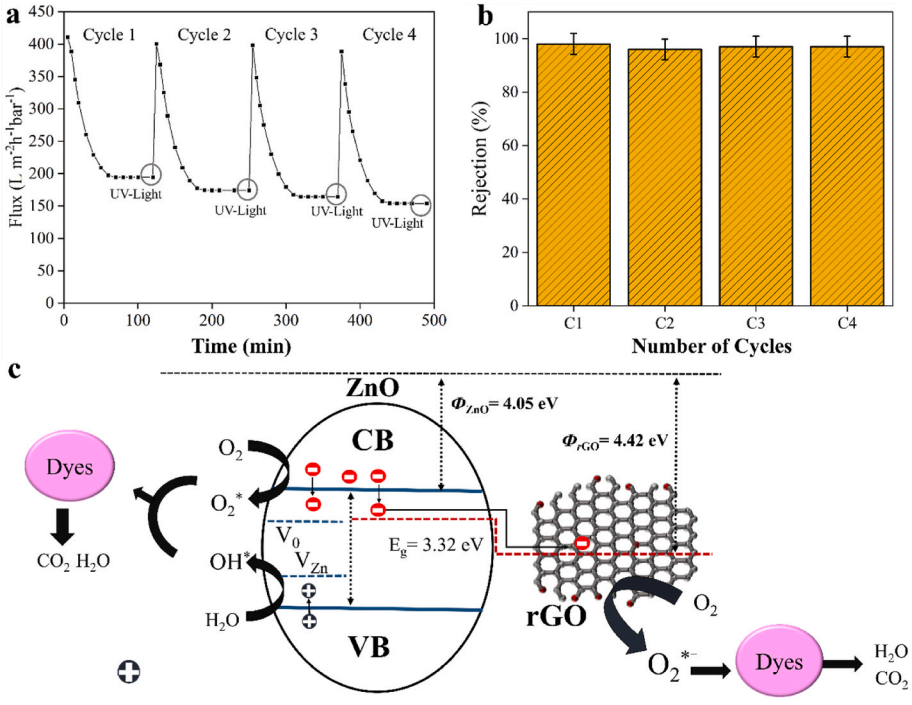

Fig. 7. (a) Cyclic experiment where the membrane was irradiated under UV–Vis light for 1 h after 120 min filtration of RB; (b) Recovery of the initial RB rejection rates for 4 cycles; and (c) Photocatalytic self-cleaning mechanism of the P-rGO/ZnO membranes.

$h^+ + H_2O \rightarrow H^+ + \bullet OH$ Eq. 14

$h^+ + OH^- \rightarrow \bullet OH$ Eq. 15

Organic contaminant $+ \bullet OH \rightarrow CO_2 + H_2O +$ other degraded products Eq. 16

Organic contaminant $+ \bullet O_2^- \rightarrow CO_2 + H_2O +$ other degraded products Eq. 17

It has been reported previously that GO-based ZnO nanocomposites exhibit high surface area, which contributes to improved pollutant adsorption. These properties appear to reduce the recombination of charge carriers and broaden the material responsiveness to visible light [92]. Overall, the membrane demonstrated highly efficient self-cleaning properties under UV–visible light irradiation, enabling excellent cyclic adsorption/desorption performance for ultrafast removal of small dyes. Therefore, this intelligent self-cleaning hybrid membrane has great potential for ultrafast wastewater purification.

4. Conclusions

In conclusion, a UV–visible light-stimulated photocatalytic self-cleaning hybrid membrane was fabricated via a direct *in-situ* self-assembly method, combining the advantages of selective rGO membrane structures and the photocatalytic properties of ZnO nanorods. The rGO layer structures act as selective layers for small molecule separation, meanwhile, the intercalated ZnO acts as space holders and endows the membrane with photocatalytic self-cleaning properties. The P-rGO/ZnO membrane exhibited a water flux up to ~400 L m^{-2} h^{-1} bar^{-1} which is 10 times higher than that of a traditional rGO membrane with a similar thickness. Meanwhile, our membrane also showed an excellent rejection rate of up to ~98.8 ± 1.2% of dye molecules that have a molecular weight >500 g mol^{-1} regardless of the dye charges. The outstanding rejection is mainly contributed by the size-sieving effect mechanism with adsorption and electrostatic interaction playing a synergetic role. Owing to the above-mentioned photocatalytic self-cleaning properties of the P-rGO/ZnO membranes, excellent cyclic dye separation performance was obtained with the water flux and dye rejection recovered up to ~95% and ~97% for every testing cycle. Overall, this work reported a unique hybrid membrane structure with self-cleaning properties and excellent cyclic separation performance for small organic molecule separation. The concept of membrane design brings new insight into the regenerable long-term membranes for ultrafast wastewater purification.

Funding sources

This work was funded by Jiangsu Dingying New Materials Co., Ltd. under Grant Number [C−00005685] and the School of Engineering, the University of Edinburgh.

CRediT authorship contribution statement

Nurul A. Mazlan: Conceptualization, Data curation, Methodology, Software, Validation, Writing – original draft, Writing – review & editing. **Allana Lewis:** Writing – review & editing. **Zheng Chen:** Writing – review & editing. **Fraz Saeed Butt:** Writing – review & editing. **Jilong Han:** Conceptualization, Writing – review & editing. **Norbert Radacsi:** Resources, Writing – review & editing. **Shuiqing Yang:** Supervision, Writing – review & editing. **Yi Huang:** Conceptualization, Funding acquisition, Methodology, Supervision, Validation, Writing – review & editing.

Declaration of competing interest

The authors declare that they have no known competing financial interests or personal relationships that could have appeared to influence the work reported in this paper.

Data availability

Data will be made available on request.

Acknowledgements

This work was funded by [Jiangsu Dingying New Materials Co., Ltd.] under Grant Number [C−00005685] and the School of Engineering, the University of Edinburgh. N.A.M. acknowledges the Malaysian Government for awarding a Ph.D. scholarship. F.S.B. thanks the Higher Education Commission of Pakistan for awarding a Ph.D. scholarship. The authors would like to thank Fergus Dingwall for his laboratory assistance and we acknowledge the use of the Zeiss Crossbeam Cryo FIB/SEM bought with the EPSRC grant EP/P030564/1 and Fraser Laidlaw for help with image acquisition.

Appendix A. Supplementary data

Supplementary data to this article can be found online at https://doi.org/10.1016/j.memsci.2024.122539.

References

[1] M.A. Shannon, P.W. Bohn, M. Elimelech, J.G. Georgiadis, B.J. Marîas, A.M. Mayes, Science and technology for water purification in the coming decades, Nature 452 (7185) (2008) 301–310, https://doi.org/10.1038/nature06599.
[2] M. Elimelech, The global challenge for adequate and safe water, J. Water Supply Res. Technol. - Aqua 55 (1) (2006) 3–10, https://doi.org/10.2166/aqua.2005.064.
[3] M. Chen, Y. Ding, Y. Liu, N. Wang, B. Yang, L. Ma, Adsorptive desulfurization of thiophene from the model fuels onto graphite oxide/metal-organic framework composites, Petrol. Sci. Technol. 36 (2) (2018) 141–147, https://doi.org/10.1080/10916466.207.1410559.
[4] X. Zhang, H. Li, J. Wang, D. Peng, J. Liu, Y. Zhang, In-situ grown covalent organic framework nanosheets on graphene for membrane-based dye/salt separation, J. Membr. Sci. 581 (2019) 321–330, https://doi.org/10.1016/j.memsci.2019.03.070.
[5] S. Sarkar, A. Banerjee, U. Halder, R. Biswas, R. Bandopadhyay, Degradation of synthetic azo dyes of textile industry: a sustainable approach using microbial enzymes, Water Conserv. Sci. Eng. 2 (4) (2017) 121–131, https://doi.org/10.1007/s41101-017-0031-5.
[6] A. Paz, J. Carballo, M.J. Pérez, J.M. Domínguez, Biological treatment of model dyes and textile wastewaters, Chemosphere 181 (2017) 168–177, https://doi.org/10.1016/j.chemosphere.2017.04.046.
[7] S.M.G.U. de Souza, L.C. Peruzzo, A.A.U. de Souza, Numerical study of the adsorption of dyes from textile effluents, Appl. Math. Model. 32 (9) (2008) 1711–1718, https://doi.org/10.1016/j.apm.2007.06.007.
[8] A. Abel, The history of dyes and pigments: from natural dyes to high-performance pigments, Colour design (2012) 557–587, https://doi.org/10.1016/B978-0-08-101270-3.00024-2.
[9] A. Pandi, G.M. Kuppuswami, K.N. Ramudu, S. Palanivel, A sustainable approach for degradation of leather dyes by a new fungal laccase, J. Clean. Prod. 211 (2019) 590–597, https://doi.org/10.1016/j.jclepro.2018.11.048.
[10] J. Kanagaraj, T. Senthilvelan, R.C. Panda, S. Kavitha, Eco-friendly waste management strategies for greener environment towards sustainable development in leather industry: a comprehensive review, J. Clean. Prod. 89 (2015) 1–17, https://doi.org/10.1016/j.jclepro.2014.11.013.
[11] E. Rosales, M. Pazos, M.A. Sanromán, Comparative efficiencies of the decolourisation of leather dyes by enzymatic and electrochemical treatments, Desalination 278 (1–3) (2011) 312–317, https://doi.org/10.1016/j.desal.2011.05.041.
[12] S.M. Ghoreishi, R. Haghighi, Chemical catalytic reaction and biological oxidation for treatment of non-biodegradable textile effluent, Chem. Eng. J. 95 (1–3) (2003) 163–169, https://doi.org/10.1016/S1385-8947(03)00100-1.
[13] A.H. Shalla, M.A. Bhat, Z. Yaseen, Hydrogels for removal of recalcitrant organic dyes: a conceptual overview, J. Environ. Chem. Eng. 6 (5) (2018) 5938–5949, https://doi.org/10.1016/j.jece.2018.08.063.
[14] Z. Cai, Y. Sun, W. Liu, F. Pan, P. Sun, J. Fu, An overview of nanomaterials applied for removing dyes from wastewater, Environ. Sci. Pollut. Res. 24 (2017) 15882–15904, https://doi.org/10.1007/s11356-017-9003-8.
[15] E. Akceylan, M. Bahadir, M. Yilmaz, Removal efficiency of a calix[4]arene-based polymer for water-soluble carcinogenic direct azo dyes and aromatic amines, J. Hazard Mater. 162 (2–3) (2009) 960–966, https://doi.org/10.1016/j.jhazmat.2008.05.127.
[16] S. Ren, D. Liu, Y. Chen, S. An, Y. Zhao, Y. Zhang, Anionic channel membrane encircled by SO_3H-polyamide 6 particles for removal of anionic dyes, J. Membr. Sci. 570 (2019) 34–43, https://doi.org/10.1016/j.memsci.2018.10.025.

[17] M. Rafatullah, O. Sulaiman, R. Hashim, A. Ahmad, Adsorption of methylene blue on low-cost adsorbents: a review, J. Hazard Mater. 177 (1–3) (2010) 70–80, https://doi.org/10.1016/j.jhazmat.2009.12.047.

[18] E. Curcio, E. Drioli, Membrane distillation and related operations - a review, Separ. Purif. Rev. 34 (1) (2005) 35–86, https://doi.org/10.1081/SPM-200054951.

[19] A. Fahmy, D. Mewes, K. Ebert, Design methodology for the optimization of membrane separation properties for hybrid vapor permeation-distillation processes, Separ. Sci. Technol. 36 (15) (2001) 3287–3304, 101081SS100107903.

[20] Y.Y. Lau, Y.S. Wong, T.T. Teng, N. Morad, M. Rafatullah, S.A. Ong, Degradation of cationic and anionic dyes in coagulation-flocculation process using bi-functionalized silica hybrid with aluminum-ferric as auxiliary agent, RSC Adv. 5 (43) (2015) 34206–34215, https://doi.org/10.1039/C5RA01346A.

[21] D. Bhatia, N.R. Sharma, J. Singh, R.S. Kanwar, Biological methods for textile dye removal from wastewater: a review, Crit. Rev. Environ. Sci. Technol. 47 (19) (2017) 1836–1876, https://doi.org/10.1080/10643389.2017.1393263.

[22] M.S. Araghi, M.E. Olya, R. Marandi, S.D. Siadat, Investigation of enhanced biological dye removal of colored wastewater in a lab-scale biological activated carbon process, Appl. Biol. Chem. 59 (3) (2016) 463–470.

[23] R. Javaid, U.Y. Qazi, Catalytic oxidation process for the degradation of synthetic dyes: an overview, Int. J. Environ. Res. Publ. Health 16 (11) (2019) 1–27. https://.org/10.1007/s13765-016-0177-4.

[24] C. Zaharia, D. Suteu, A. Muresan, R. Muresan, A. Popescu, Textile wastewater treatment by homogeneous oxidation with hydrogen peroxide, Environ. Eng. Manag. J. 8 (6) (2009) 1359–1369. https://.org/10.30638/eemj.2009.199.

[25] L. Cheng, M. Wei, L. Huang, F. Pan, D. Xia, X. Li, and A. Hu, Efficient H_2O_2 oxidation of organic dyes catalyzed by simple copper(II) ions in bicarbonate aqueous solution, Ind. Eng. Chem. Res. 53 (9) 3478–3485, https://doi.org/10.1021/ie403801f.

[26] M.T. Yagub, T.K. Sen, S. Afroze, H.M. Ang, Dye and its removal from aqueous solution by adsorption: a review, Adv. Colloid Interface Sci. 209 (2014) 172–184, https://doi.org/10.1016/j.cis.2014.04.002.

[27] C.Z. Liang, S.P. Sun, F.Y. Li, Y.K. Ong, T.S. Chung, Treatment of highly concentrated wastewater containing multiple synthetic dyes by a combined process of coagulation/flocculation and nanofiltration, J. Membr. Sci. 469 (2014) 306–315, https://doi.org/10.1016/j.memsci.2014.06.057.

[28] K.O. Agenson, J.I. Oh, T. Urase, Retention of a wide variety of organic pollutants by different nanofiltration/reverse osmosis membranes: controlling parameters of process, J. Membr. Sci. 225 (1–2) (2003) 91–103, https://doi.org/10.1016/j.memsci.2003.08.006.

[29] H. Yu, Y. He, G. Xiao, Y. Fan, J. Ma, Y. Gao, R. Hou, X. Yin, Y. Wang, X. Mei, The roles of oxygen-containing functional groups in modulating water purification performance of graphene oxide-based membrane, Chem. Eng. J. 389 (2020) 124375, https://doi.org/10.1016/j.cej.2020.124375.

[30] Y. Gao, Y. He, S. Yan, H. Yu, J. Ma, R. Hou, Y. Fan, Controlled reduction and fabrication of graphene oxide membrane for improved permeance and water purification performance, J. Mater. Sci. 55 (31) (2020) 15130–15139, https://doi.org/10.1007/s10853-020-05073-9.

[31] N. Wei, X. Peng, Z. Xu, Understanding water permeation in graphene oxide membranes, ACS Appl. Mater. Interfaces 6 (8) (2014) 5877–5883, https://doi.org/10.1021/am500777b.

[32] P. Su, F. Wang, Z. Li, C.Y. Tang, W. Li, Graphene oxide membranes: controlling their transport pathways, J. Mater. Chem. A 8 (31) (2020) 15319–15340, https://doi.org/10.1039/D0TA02249G.

[33] W. Wu, Y. Shi, G. Liu, X. Fan, Y. Yu, Recent development of graphene oxide based forward osmosis membrane for water treatment: a critical review, Desalination 491 (2020) 114452, https://doi.org/10.1016/j.desal.2020.114452.

[34] D.R. Dreyer, S. Park, C.W. Bielawski, R.S. Ruoff, The chemistry of graphene oxide, Chem. Soc. Rev. 39 (1) (2010) 228–240, https://doi.org/10.1039/B917103G.

[35] G. Eda, G. Fanchini, M. Chhowalla, Large-area ultrathin films of reduced graphene oxide as a transparent and flexible electronic material, Nat. Nanotechnol. 3 (5) (2008) 270–274. http://www.nature.com/doifinder/10.1038/nnano.2008.83.

[36] T.A. Makhetha, R.M. Moutloali, Antifouling properties of Cu(tpa)@GO/PES composite membranes and selective dye rejection, J. Membr. Sci. 554 (2018) 195–210, https://doi.org/10.1016/j.memsci.2018.03.003.

[37] X. Wen, T. Foller, X. Jin, T. Musso, P. Kumar, R. Josho, Understanding water transport through graphene based nanochannels via experimental control of slip length, Nat. Commun. 13 (1) (2022) 5690, https://doi.org/10.1038/s41467-022-33456-w.

[38] Q. Kong, X. Shi, W. Ma, F. Zhang, T. Yu, F. Zhao, D. Zhao, C. Wei, Strategies to improve the adsorption properties of graphene-based adsorbent towards heavy metal ions and their compound pollutants: a review, J. Hazard Mater. 415 (2021) 125690, https://doi.org/10.1016/j.jhazmat.2021.125690.

[39] Y. Li, W. Zhao, M. Weyland, S. Yuan, Y. Xia, H. Liu, M. Jian, J. Yang, C.D. Easton, C. Selomulya, X. Zhang, Thermally reduced nanoporous graphene oxide membrane for desalination, Environ. Sci. Technol. 53 (14) (2019) 8314–8323, https://doi.org/10.1021/acs.est.9b01914.

[40] J.R. Werber, C.O. Osuji, M. Elimelech, Materials for next-generation desalination and water purification membranes, Nat. Rev. Mater. 1 (5) (2016) 1–15, https://doi.org/10.1038/natrevmats.2016.18.

[41] K. Flores, C. Valdes, D. Ramirez, T.M. Eubanks, J. Lopez, C. Hernandez, M. Alcoutlabi, J.G. Parsons, The effect of hybrid zinc oxide/graphene oxide (ZnO/GO) nano-catalysts on the photocatalytic degradation of simazine, Chemosphere 259 (2020) 127414, https://doi.org/10.1016/j.chemosphere.2020.127414.

[42] Y. Gao, M. Hu, B. Mi, Membrane surface modification with TiO_2-graphene oxide for enhanced photocatalytic performance, J. Membr. Sci. 455 (2014) 349–356, https://doi.org/10.1016/j.memsci.2014.01.011.

[43] Y. Mao, Q. Huang, B. Meng, K. Zhou, G. Liu, A. Gugliuzza, E. Drioli, W. Jin, Roughness-enhanced hydrophobic graphene oxide membrane for water desalination via membrane distillation, J. Membr. Sci. 611 (2020) 118364, https://doi.org/10.1016/j.memsci.2020.118364.

[44] A. Xie, J. Cui, J. Yang, Y. Chen, J. Lang, C. Li, Y. Yan, J. Dai, Graphene oxide/Fe (III)-based metal-organic framework membrane for enhanced water purification based on synergistic separation and photo-Fenton processes, Appl. Catal., B 264 (2020) 118548, https://doi.org/10.1016/j.apcatb.2019.118548.

[45] J. Ma, X. Guo, Y. Ying, D. Liu, C. Zhong, Composite ultrafiltration membrane tailored by MOF@GO with highly improved water purification performance, Chem. Eng. J. 313 (2017) 890–898, https://doi.org/10.1016/j.cej.2016.10.127.

[46] S. Yang, Q. Zou, T. Wang, L. Zhang, Effects of GO and MOF@GO on the permeation and antifouling properties of cellulose acetate ultrafiltration membrane, J. Membr. Sci. 569 (2019) 48–59, https://doi.org/10.1016/j.memsci.2018.09.068.

[47] R. Heu, M. Ateia, C. Yoshimura, Photocatalytic nanofiltration membrane using Zr-MOF/GO nanocomposite with high-flux and anti-fouling properties, Catalysts 10 (6) (2020) 711, https://doi.org/10.3390/catal10060711.

[48] C. Li, Q. Yang, D. Liu, H. Nie, Y. Liu, Removal of organic phosphonate HEDP by Eu-MOF/GO composite membrane, J. Environ. Chem. Eng. 9 (6) (2021) 106895, https://doi.org/10.1016/j.jece.2021.106895.

[49] V. A. Ganesh, H. K. Raut, A. S. Nair, S. Ramakrishna, A review on self-cleaning coatings, J. Mater. Chem. 21 (41) (201) 16304–16322, https://doi.org/10.1039/C1JM12523K.

[50] M.Y. Guo, M.K. Fun, F. Fang, X.Y. Chen, A.M.C. Ng, A.B. Djurisic, W.K. Chan, ZnO and TiO2 1D nanostructures for photocatalytic applications, J. Alloys Compd. 509 (4) (2011) 1328–1332, https://doi.org/10.1016/j.jallcom.2010.10.028.

[51] Y. Sun, G.M. Fuge, M.N.R. Ashfold, Growth of aligned ZnO nanorod arrays by catalyst-free pulsed laser deposition methods, Chem. Phys. Lett. 396 (1–3) (2004) 21–26, https://doi.org/10.1016/j.cplett.2004.07.110.

[52] J.J. Wu, S.C. Liu, Low-temperature growth of well-aligned ZnO nanorods by chemical vapor deposition, Adv. Mater. 14 (3) (2002) 215–218, https://doi.org/10.1002/1521-4095(20020205)14:3%3C215::AID-ADMA215%3E3.0.CO;2-J.

[53] Y.K. Mishra, S. Kaps, A. Schuchardt, I. Paulowicz, X. Jin, D. Gedam, Fabrication of macroscopically flexible and highly porous 3D semiconductor networks from interpenetrating nanostructures by a simple flame transport approach, Part. Part. Syst. Char. 30 (9) (2013) 775–783, https://doi.org/10.1002/2Fppsc.201300197.

[54] N. Li, W. Wang, C. Ma, L. Zhu, X. Chen, B. Zhang, C. Zhong, A novel conductive rGO/ZnO/PSF membrane with superior water flux for electrocatalytic degradation of organic pollutants, J. Membr. Sci. 641 (2022) 119901, https://doi.org/10.1016/j.memsci.2021.119901.

[55] N.A.F. Al-Rawashdeh, O. Allabadi, M.T. Aljarrah, Photocatalytic activity of graphene oxide/zinc oxide nanocomposites with embedded metal nanoparticles for the degradation of organic dyes, ACS Omega 5 (43) (2020) 28046–28055, https://doi.org/10.1021/acsomega.0c03608.

[56] Q. Wang, J. Cui, A. Xie, J. Lang, C. Li, Y. Yan, PVDF composite membrane with robust UV-induced self-cleaning performance for durable oil/water emulsions separation, J. Taiwan Inst. Chem. Eng. 110 (2020) 130–139, https://doi.org/10.1016/j.memsci.2021.119901.

[57] T. Chen, F.S. Butt, M. Zhang, X. Wei, A. Lewis, N. Radacsi, A.J.C. Semiao, J. Han, Y. Huang, Ultra-permeable zeolitic imidazolate frameworks-intercalated graphene oxide membranes for unprecedented ultrafast molecular separation, Chem. Eng. J. 419 (2021) 129507, https://doi.org/10.1016/j.cej.2021.129507.

[58] S. Park, K.S. Lee, G. Bozoklu, W. Cai, S.B.T. Nguyen, R.S. Ruoff, Graphene oxide papers modified by divalent ions - enhancing mechanical properties via chemical cross-linking, ACS Nano 2 (3) (2008) 572–578, https://doi.org/10.1021/nn700349a.

[59] H. Wang, X. Yuan, Y. Wu, H. Huang, G. Zeng, Y. Liu, X. Wang, N. Lin, Y. Qi, Adsorption characteristics and behaviors of graphene oxide for Zn(II) removal from aqueous solution, Appl. Surf. Sci. 279 (2013) 432–440, https://doi.org/10.1016/j.apsusc.2013.04.133.

[60] R.B. d'Água, B. Branquinho, R. Duarte, M.P. Mauricio, E. Fernando, A.L. Martins, E. Fortunato, Efficient coverage of ZnO nanoparticles on cotton fibres for antibacterial finishing using a rapid and low cost: in situ synthesis, New J. Chem. 42 (2) (2018) 1052–1060, https://doi.org/10.1039/C7NJ03418K.

[61] A. Jilani, M.Sh Abdel-Wahab, H.Y. Zahran, I.S. Yahia, A.A. Al-Ghamdi, A. Alshahrie, A.M. El-Naggar, Chemical state analysis, optical band gap, and photocatalytic decolorization of cobalt-doped ZnO nanospherical thin films by DC/RF sputtering technique, Optik 164 (2018) 143–154, https://doi.org/10.1016/j.ijleo.2018.02.073.

[62] R.S. Yadav, P. Mishra, A.C. Pandey, Growth mechanism and optical property of ZnO nanoparticles synthesized by sonochemical method, Ultrason. Sonochem. 15 (5) (2008) 863–868, https://doi.org/10.1016/j.ultsonch.2007.11.003.

[63] Y.v. Il'ichev, J.D. Simon, Building blocks of Eumelanin: relative stability and excitation energies of tautomers of 5,6-dihydroxyindole and 5,6-indolequinone, J. Phys. Chem. B 107 (29) (2003) 7162–7171, https://doi.org/10.1021/jp034702x.

[64] Z.Y. Xi, Y.Y. Xu, L.P. Zhu, Y. Wang, B.K. Zhu, A facile method of surface modification for hydrophobic polymer membranes based on the adhesive behavior of poly(DOPA) and poly(dopamine), J. Membr. Sci. 327 (1–2) (2009) 244–253, https://doi.org/10.1016/j.memsci.2008.11.037.

[65] S. Park, D.A. Dikin, S.T. Nguyen, R.S. Ruoff, Graphene oxide sheets chemically cross-linked by polyallylamine, J. Phys. Chem. C 113 (36) (2009) 15801–15804, https://doi.org/10.1021/jp907613s.

[66] L.C. Lin, J.C. Grossman, Atomistic understandings of reduced graphene oxide as an ultrathin-film nanoporous membrane for separations, Nat. Commun. 6 (1) (2015) 8335, https://doi.org/10.1038/ncomms9335.

[67] R. Shi, P. Yang, X. Dong, Q. Ma, A. Zhang, Growth of flower-like ZnO on ZnO nanorod arrays created on zinc substrate through low-temperature hydrothermal synthesis, Appl. Surf. Sci. 264 (2013) 162–170, https://doi.org/10.1016/j.apsusc.2012.09.164.
[68] R.C. Pawar, C.S. Lee, Single-step sensitization of reduced graphene oxide sheets and CdS nanoparticles on ZnO nanorods as visible-light photocatalysts, Appl. Catal., B 144 (1) (2014) 57–65, https://doi.org/10.1016/j.apcatb.2013.06.022.
[69] W.D. Yang, Y.R. Li, Y.C. Lee, Synthesis of r-GO/TiO 2 composites via the UV-assisted photocatalytic reduction of graphene oxide, Appl. Surf. Sci. 380 (2016) 249–256, https://doi.org/10.1016/j.apsusc.2016.01.118.
[70] A. Morelos-Gomez, R. Cruz-Silva, H. Muramatsu, J. Ortiz-Medina, T. Araki, T. Fukuyo, S. Tejima, K. Takeuchi, T. Hayashi, M. Terrones, M. Endo, Effective NaCl and dye rejection of hybrid graphene oxide/graphene layered membranes, Nat. Nanotechnol. 12 (11) (2017) 1083–1088, https://doi.org/10.1038/nnano.2017.160.
[71] M. Amini, M. Seifi, A. Akbari, M. Hosseinifard, Polyamide-zinc oxide-based thin film nanocomposite membranes: towards improved performance for forward osmosis, Polyhedron 179 (2020) 114362, https://doi.org/10.1016/j.poly.2020.114362.
[72] P. Peechmani, M.H.D. Othman, R. Kamaludin, M.H. Puteh, J. Jaafar, M.A. Rahman, A.F. Ismail, S.H.S.A. Kadir, R.M. Illias, J. Gallagher, S.M. Djuli, High flux polysulfone braided hollow fiber membrane for wastewater treatment role of zinc oxide as hydrophilic enhancer, J. Environ. Chem. Eng. 9 (5) (2021) 105873, https://doi.org/10.1016/j.jece.2021.105873.
[73] N.A. Patankar, Supernucleating surfaces for nucleate boiling and dropwise condensation heat transfer, Soft Matter 6 (8) (2010) 1613–1620, https://doi.org/10.1039/B923967G.
[74] C. Wang, Z. Li, J. Chen, Y. Yin, H. Wu, Structurally stable graphene oxide-based nanofiltration membranes with bioadhesive polydopamine coating, Appl. Surf. Sci. 427 (2018) 1092–1098, https://doi.org/10.1016/j.apsusc.2017.08.124.
[75] P. Zhang, J.L. Gong, G.M. Zeng, B. Song, H.Y. Liu, S.Y. Huan, J. Li, Ultrathin reduced graphene oxide/MOF nanofiltration membrane with improved purification performance at low pressure, Chemosphere 204 (2018) 378–389, https://doi.org/10.1016/j.chemosphere.2018.04.064.
[76] X. Fan, C. Cai, J. Gao, X. Han, J. Li, Hydrothermal reduced graphene oxide membranes for dyes removing, Sep. Purif. Technol. 241 (2020) 116730, https://doi.org/10.1016/j.seppur.2020.116730.
[77] R. Zhang, Y. Cai, X. Zhu, Q. Han, T. Zhang, Y. Liu, Y. Li, A. Wang, A novel photocatalytic membrane decorated with PDA/RGO/Ag_3PO_4 for catalytic dye decomposition, Colloids Surf., A 563 (2019) 68–76, https://doi.org/10.1016/j.colsurfa.2018.11.069.
[78] G. Liu, W. Jin, N. Xu, Graphene-based membranes, Chem. Soc. Rev. 44 (15) (2015) 5016–5030, https://doi.org/10.1039/C4CS00423J.
[79] C.Y. Wang, W.J. Zeng, T.T. Jiang, X. Chen, X.L. Zhang, Incorporating attapulgite nanorods into graphene oxide nanofiltration membranes for efficient dyes wastewater treatment, Sep. Purif. Technol. 214 (2019) 21–30, https://doi.org/10.1016/j.seppur.2018.04.079.
[80] A. Degen, M. Kosec, Effect of pH and impurities on the surface charge of zinc oxide in aqueous solution, J. Eur. Ceram. Soc. 20 (6) (2000) 667–673, https://doi.org/10.1016/S0955-2219(99)00203-4.
[81] X. Ou, X. Yang, J. Zheng, M. Liu, Free-standing graphene oxide-chitin nanocrystal composite membrane for dye adsorption and oil/water separation, ACS Sustain. Chem. Eng. 7 (15) (2019) 13379–13390, https://doi.org/10.1021/acssuschemeng.9b02619.
[82] Y.H. Xi, J.Q. Hu, Z. Liu, R. Xie, X.J. Ju, W. Wang, L.Y. Chu, Graphene oxide membranes with strong stability in aqueous solutions and controllable lamellar spacing, ACS Appl. Mater. Interfaces 8 (24) (2016) 15557–15566, https://doi.org/10.1021/acsami.6b00928.
[83] B. Liang, P. Zhang, J. Wang, J. Qu, L. Wang, X. Wang, C. Guan, K. Pan, Membranes with selective laminar nanochannels of modified reduced graphene oxide for water purification, Carbon 103 (2016) 94–100, https://doi.org/10.1016/j.carbon.2016.03.001.
[84] C.J. Wang, H.C. You, K. Lin, J.H. Ou, K.H. Chao, F.H. Ko, Highly transparent and Surface-Plasmon-Enhanced visible-photodetector based on zinc oxide thin-film transistors with heterojunction structure, Materials 12 (2019) 3639, https://doi.org/10.3390/ma12213639.
[85] W. Yuan, C. Li, T. Chu, M. Cheng, S. Hou, In-situ chemical formation of strong stability GO/rGO hybrid membranes for efficient treatment of organic pollutant, Mater. Lett. 314 (2022) 131849, https://doi.org/10.1016/j.matlet.2022.131849.
[86] J.A. Rogers, A.A. Maznev, M.J. Banet, K.A. Nelson, Optical generation and characterization of acoustic waves in thin films: fundamentals and applications, Annu. Rev. Mater. Sci. 30 (2000) 117–157, https://doi.org/10.1146/annurev.matsci.30.1.117.
[87] C.F. Liu, Y.J. Lu, C.C. Hu, Effects of anions and pH on the stability of ZnO nanorods for photoelectrochemical water splitting, ACS Omega 3 (2018) 3429–3439, https://doi.org/10.1021/acsomega.8b00214.
[88] M.O. Fatehah, H.A. Aziz, S. Stoll, Stability of ZnO nanoparticles in solution. Influence of pH, dissolution, aggregation and disaggregation effects, J. Colloid Sci. Biotechnol. 3 (2014) 75–84, https://doi.org/10.1166/jcsb.2014.1072.
[89] Y. Han, D. Kim, G. Hwang, B. Lee, I. Eom, P.J. Kim, M. Tong, H. Kim, Aggregation and dissolution of ZnO nanoparticles synthesized by different methods: influence of ionic strength and humic acid, Colloids Surf., A 451 (2014) 7–15, https://doi.org/10.1016/j.colsurfa.2014.03.030.
[90] S.K. Mandal, K. Dutta, S. Pal, S. Mandal, A. Naskar, P.K. Pal, T.S. Bhattacharya, A. Singha, R. Saikh, S. De, D. Jana, Engineering of ZnO/rGO nanocomposite photocatalyst towards rapid degradation of toxic dyes, Mater. Chem. Phys. 223 (2019) 456–465, https://doi.org/10.1016/j.matchemphys.2018.11.002.
[91] A.A. Yaqoob, N. Habibah, A. Serr, M. Nasir, M. Ibrahim, Advances and challenges in developing efficient graphene oxide-based ZnO photocatalysts for dye photo-oxidation, Nanomaterials 10 (2020) 32, https://doi.org/10.3390/nano10050932.
[92] H.N. Tien, V.H. Luan, L.T. Hoa, N.T. Khoa, S.H. Hahn, J.S. Chung, E.W. Shin, S. H. Hur, One-pot synthesis of a reduced graphene oxide-zinc oxide sphere composite and its use as a visible light photocatalyst, J. Chem. Eng. 229 (2013) 126–133, https://doi.org/10.1016/j.cej.2013.05.110.
[93] C. Rodwihok, D. Wongratanaphisan, Y.L.T. Ngo, M. Khandelwal, S.H. Hur, J. S. Chung, Effect of GO additive in ZnO/rGO nanocomposites with enhanced photosensitivity and photocatalytic activity, Nanomaterials 9 (2019) 1441, https://doi.org/10.3390/nano9101441.